MODELING THE EFFECTS OF THREE-DIMENSIONAL PORE GEOMETRY ON

GAS HYDRATE PHASE STABILITY

by

JULIA TONGE IRIZARRY

A THESIS

THESIS APPROVAL PAGE

Student: Julia Tonge Irizarry

Title: Modeling the Effects of Three-Dimensional Pore Geometry on Gas Hydrate Phase Stability

This thesis has been accepted and approved in partial fulfillment of the requirements for the Master of Science degree in the Department of Geological Sciences by:

Alan Rempel   Chairperson
David Sutherland   Member
Mark H. Reed   Member

and

Scott L. Pratt   Dean of the Graduate School

Original approval signatures are on file with the University of Oregon Graduate School.

Degree awarded June 2015

THESIS ABSTRACT

Julia Tonge Irizarry

Master of Science

Department of Geological Sciences

June 2015

Title: Modeling the Effects of Three-Dimensional Pore Geometry on Gas Hydrate Phase
Stability

Porous media affect hydrate stability by forcing hydrate-liquid interfaces to form

high curvature geometries and by forcing the molecules of the hydrate, liquid, and

sedimentary particles that compose the medium to interact where they are in close

proximity. To evaluate these effects we first create synthetic spherical packings to

approximate pore space geometry. We use the synthetic pore space to calculate the

perturbation to the chemical potential caused by the geometrical constraints. Our model

predictions agree with published data for ice-water and water-vapor systems. When

particles are well-approximated as spheres, our model fits the data with R-squared values

that range between about 80% to over 99%. However, our model needs to be improved for

porous media that contain a significant fraction of non-equant particles such as clay. Lastly,

we demonstrate how our model can be used in predictions for the evolution of hydrate

saturation.

This thesis includes unpublished co-authored material.

CURRICULUM VITAE

NAME OF AUTHOR: Julia Tonge Irizarry

GRADUATE AND UNDERGRADUATE SCHOOLS ATTENDED:

    University of Oregon, Eugene
    Appalachian State University, Boone, NC
    University of North Carolina at Charlotte, Charlotte, NC

DEGREES AWARDED:

    Master of Science, Geological Sciences, 2015, University of Oregon
    Bachelor of Science, Geology: Quantitative Geoscience, 2013, Appalachian State
        University

AREAS OF SPECIAL INTEREST:

    Geophysics

    Computational geology

    Fluid-particle interactions

PROFESSIONAL EXPERIENCE:

    Graduate Research Assistant, University of Oregon, 2013-2015

    Graduate Teaching Fellow, University of Oregon, 2013-2015

GRANTS, AWARDS, AND HONORS:

    Johnston Scholarship in Geophysics and Structural Geology, Department of
        Geological Sciences, University of Oregon, 2014

    Geology Student of the Year Award, Appalachian State University, 2013

    Quantitative Geoscience Major Student of the Year Award, Appalachian State
        University, 2013

    Undergraduate Student Research Award, "Static Stress Changes Due to the 1994
        M6.7 Northridge Earthquake and the Potential for Triggered Slip on the San
        Andreas Fault," Appalachian State University, 2011

    Undergrad Research Assistance Award, Appalachian State University, 2011

ACKNOWLEDGMENTS

For my wonderful parents.

TABLE OF CONTENTS

LIST OF FIGURES

LIST OF TABLES

CHAPTER I

INTRODUCTION

The material presented in this thesis is in preparation for publication with Alan Rempel as coauthor.

Gas hydrates are ice-like compounds that form on continental shelves from mixtures of methane and water. The sedimentary particles hosting the gas hydrates modify the two-phase equilibrium conditions of the hydrate-liquid system (Clennell et al., 1999; Cook and Malinverno, 2013; Daigle and Dugan, 2011; Rempel, 2011). The phase equilibrium shifts from bulk phase equilibrium for two primary reasons: first, because the complex pore geometry forces the hydrate-liquid interface to curve (**Fig. 1**) and have higher surface energy than in a planar geometry, and second, because of the intermolecular forces that induce liquid water to wet the interfaces between sediment particles and hydrate crystals (Rempel, 2011). Similar behavior occurs in vapor-water systems, where the pore fraction occupied by liquid, or liquid saturation, depends on the matric potential, which is defined as the pressure difference between the non-wetting vapor phase and the wetting liquid phase (e.g. Or and Tuller, 1999). In ice-water systems the effects of curvature and wetting facilitate the stable equilibrium presence of residual liquid with a saturation that depends on the undercooling ΔT, which is defined as the temperature depression below the normal melting point (e.g. Rempel, 2012). Our focus is on hydrate behavior, but we mention these other systems here, because we use them

below in tests to validate our numerical procedure. Below, we describe our approach, model validation tests, and how our model can be applied to the hydrate-liquid system.

We developed a computational method for predicting the shift in phase equilibrium in three-dimensional porous media. Our codes are designed to: a) synthetically produce a sphere packing of poly-dispersed particles with a specified size distribution, b) determine the geometrical constraints on hydrate phase-equilibrium at any given point within the pore space, and c) quantify the effects of these constraints in modifying the phase behavior for a specified model.

Several models have been developed that simplify the pore geometry while still capturing some effects of the porous medium on phase behavior. Pore geometry is most commonly modeled by approximating pores as circular cylinders (Denoyel and Pellenq, 2002; Millington and Quirk, 1961; Mualem, 1976; Wilder et al., 2001). Other approaches include the use of circular pores connected by narrower pore throats (Liu and Flemings, 2011), triangular pores (Rempel, 2011), and random packings of circles (Rempel, 2012). To extend beyond these two-dimensional idealizations, we develop a sphere-packing tool in MATLAB that creates a three-dimensional packing to emulate the arrangement of sedimentary particles. We use the three-dimensional pore geometry created by the to predict the perturbations to the phase behavior that result. Even for idealized simple cubic and face-centered cubic packing, fully evaluating the shape of the evolving three-dimensional interphase geometry can be prohibitively complex (Cahn et al., 1992). We avoid calculating the detailed geometry of the hydrate phase within each individual pore by sampling at discrete points within the synthetic pore space and instead focus only on the local geometry of the phase interface when it first intersects each sampled location.

2
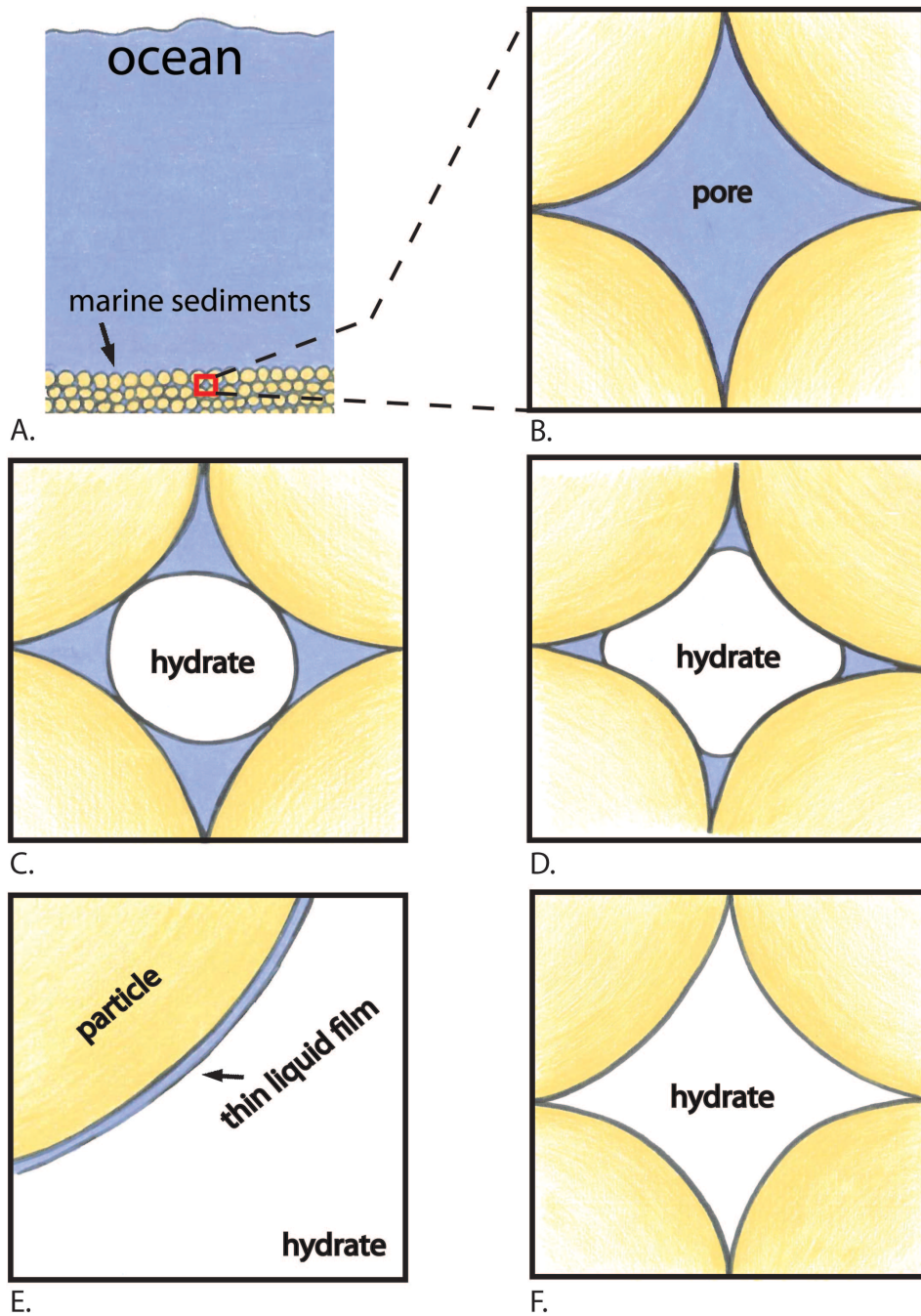
Fig. 1. Diagram depicting the geometry of hydrate filling a pore. (A) Shows sedimentary particles at the seafloor. (B) A simplification of the non-planar geometry introduced by particle contacts. (C) The first hydrate crystal to a form within a pore is approximately the shape of the largest sphere that can fit within the pore. (D) The hydrate continues to grow into the crevices between particle contacts. (E) Even with increased cooling, liquid phase remains connected by thin liquid films that coat the particle surfaces. (F) At very low temperatures the final residual liquid disappears.

3

The pore-scale effects we examine can create small gas solubility differences between adjacent coarse and fine-grained sedimentary layers. Previous studies associate the occurrence of hydrate anomalies (sharp increases in hydrate saturation) with the stratified arrangement of layers containing coarse particles sandwiched between layers containing finer particles (Clennell et al., 1999; Cook and Malinverno, 2013; Daigle and Dugan, 2011; Rempel, 2011). These gas hydrate anomalies are not simply controlled by the well-understood effects of temperature, pressure, and salinity on hydrate and liquid phase behavior. Instead the formation and behavior of these anomalies depend on the micro-scale effects and interactions between the ice-like hydrate and the intricate pore geometry dictated by the encompassing porous medium. In our study, we quantify how the gas solubility changes as differences in particle-size distributions are encountered; this information can be used in reactive transport models for the evolution of gas hydrate deposits. We provide an example of this in **Section 5,** where we predict the saturation of a hydrate anomaly given particle size distribution data and a few other input parameters required to characterize the site at which the hydrate was found (Rose et al., 2014).

CHAPTER II

GUIDING PRINCIPLES

In the case of a hydrate-liquid system, we are interested in how the disturbance to the phase equilibrium causes changes in the equilibrium solubility of methane dissolved in the aqueous solution adjacent to hydrate crystals. Once we determine the undercooling ΔT that is produced by pore-scale effects, we can calculate the modification to the equilibrium concentration as

$$c_{eq} \approx c_{bulk}\, exp(\tfrac{\Delta T}{\alpha}),\tag{1}$$

where c_{bulk} is the equilibrium concentration of the bulk solution neglecting porous medium effects at the *in situ* temperature and pressure, and the scaling temperature $\alpha = 14.4°C$ for methane hydrate in salt-free water (Davie et al., 2004).

In **Section 4**, we use laboratory data from ice-water and water-vapor systems to validate our modeling approach through comparisons against predicted changes in undercooling and matric potential. The process of predicting disturbances to the chemical potential in the ice-water and water-vapor systems is the same as predicting chemical potential disturbances in the hydrate-liquid system, for which there are comparatively little data. However, the shifts in chemical equilibrium in the ice-water and water-vapor systems, are typically measured in terms of the undercooling and matric potential, respectively, whereas we are interested in c_{eq}.

2.1. Phase Pressure Difference

Our focus is drawn to natural gas hydrate systems that aggregate over periods of centuries to millennia, allowing sufficient time to reach equilibrium phase distributions. We begin with a brief review of the well-understood ways that pore characteristics modify phase equilibrium. Starting at a reference state with bulk melting temperature T_m and pressure P_m, equilibrium implies that

$$\mu_w(T_m, P_m) = \mu_{nw}(T_m, P_m), \tag{2}$$

where μ is the chemical potential, and the subscript w denotes a wetting phase variable, whereas nw denotes a non-wetting phase variable. The wetting phase against the sediment particles is assumed to be liquid water and the non-wetting phase may refer to hydrate, ice, or water vapor. Now we use the Gibbs-Duhem equation to write the following equalities describing the chemical potentials of the wetting and non-wetting phase in a perturbed state

$$\mu_w(T, P_w) = \mu_w(T_m, P_m) - s_w(T - T_m) + v_w(P_w - P_m), \tag{3}$$

and

$$\mu_{nw}(T, P_{nw}) = \mu_{nw}(T_m, P_m) - s_{nw}(T - T_m) + v_{nw}(P_{nw} - P_m), \tag{4}$$

where s is the specific entropy and v is the specific volume (Kofke, 1993; Lomba et al., 1996; Rempel et al., 2001) Equilibrium implies that we can equate the chemical

6

potentials along the phase boundary, where T is the same in each phase but the phase

pressures can be different, i.e. $P_w \neq P_{nw}$, so that

$$0 = (-s_w + s_{nw})(T - T_m) + v_{nw}(P_w - P_{nw}) + (v_w - v_{nw})(P_w - P_m). \tag{5}$$

We introduce the latent heat L and densities ρ so that we can substitute

$$s_w - s_{nw} \approx \frac{L}{T_m}, \tag{6}$$

$$v_{nw} = \frac{1}{\rho_{nw}}, \tag{7}$$

and

$$v_w = \frac{1}{\rho_w} \tag{8}$$

to arrive at

$$0 = \frac{-L}{T_m}(T - T_m) - \frac{1}{\rho_{nw}}(P_{nw} - P_w) + (\frac{1}{\rho_w} - \frac{1}{\rho_{nw}})(P_w - P_m). \tag{9}$$

To focus on the effects of the porous medium in modifying the phase behavior, we set the

pressure in the wetting phase equal to the reference pressure P_m that defines the bulk

melting temperature T_m and rearrange equation (9) to obtain

$$\frac{\rho_{nw}L}{T_m}(T_m - T) = \frac{\rho_{nw}L}{T_m}\Delta T = P_{nw} - P_m = P_{nw} - P_w. \tag{10}$$

7

2.2. Incorporation of Curvature Effects

We can use equation (10) to calculate the perturbation that has occurred to phase equilibrium due to enhanced pressure in the solid phase that arises from curvature and wetting effects. First we consider the curvature effects, using Laplace's equation (Laplace, 1831)

$$\Delta P = P_{nw} - P_w = \gamma \kappa = \gamma \left(\frac{1}{r_1} + \frac{1}{r_2} \right). \tag{11}$$

Here, γ is the surface energy of the phase interface, κ is the curvature of the phase interface, and r_1 and r_2 are the principle radii of curvature along the phase interface. For a sphere $r_1 = r_2$, therefore across a spherical interface

$$\Delta P = \frac{2\gamma}{r}. \tag{12}$$

Equation (12) will be useful when the hydrate crystals can approximated as spheres, and also as a component of the calculation for the thin films that conform to the surfaces of the sediment particles, which we approximate as spheres.

2.3. Incorporation of Liquid Film

Next we account for the presence of thin liquid films that remain coated on particles far below the bulk melting temperature, often referred to as premelt or premelted films (Dash et al., 2006; Rempel et al., 2001). *Israelachvili* (2011) has exhaustively studied the details of wetting phenomena, but the thickness of liquid films are commonly

described by a simple power-law equation (Cahn et al., 1992; Elbaum and Schick, 1995; Garvin and Udaykumar, 2006; Rempel and Worster, 1999; Tuller and Or, 2005; Watanabe and Mizoguchi, 2002). Other functional forms are possible, however, the qualitative behavior is always the same insofar as the film thickness must decrease as the pressure difference between the two phases is enhanced (Bischof et al., 1996; De Gennes, 1985; Hansen-Goos and Wettlaufer, 2010; Rempel et al., 2001). In this study, we account for wetting interactions using

$$\Delta P = P_0 (\frac{\lambda_0}{d})^\beta, \tag{13}$$

where β is controlled by the dominant microphysical interactions and is treated as constant, d is the thickness of the liquid film, and λ_0 is the film thickness at reference pressure P_0. By combining the wetting effects with the curvature effects from equation (11), we have the general relationship

$$\Delta P = \gamma \kappa + P_0 (\frac{\lambda_0}{d})^\beta = \gamma (\frac{1}{r_1} + \frac{1}{r_2}) + P_0 (\frac{\lambda_0}{d})^\beta, \tag{14}$$

which is the pressure jump across a curved interface separated by distance d from a particle surface. Now we can adapt this general relationship to describe the specific problem of wetting on the surface of a particle with radius R_p so that the two principle radii of curvature $r_1 = r_2 = -R_p$, which implies that

$$\Delta P = P_0 (\frac{\lambda_0}{d})^\beta - \frac{2\gamma}{R_p}. \tag{15}$$

Equation (15) is equivalent to the matric potential along the thin films that coat sediment particles in a liquid-vapor system. By substituting equation (15) into equation (10) we can describe the undercooling along a wetting film interface for an ice-liquid system, as

$$\frac{\rho_{nw}L}{T_m}\Delta T = P_0(\frac{\lambda_0}{d})^\beta - \frac{2\gamma}{R_p}.$$

(16)

For hydrates we are interested in the shift in solubility from the bulk equilibrium concentration c_{bulk}, to a new equilibrium concentration c_{eq}, because this shift in dissolved methane content can cause hydrate anomalies to form. Substituting equation (16) into equation (1), the equilibrium concentration can be described by

$$c_{eq} \approx c_{bulk}exp(\frac{\Delta T}{\alpha}) \approx c_{bulk}exp\left\{\frac{T_m}{\rho_{nw}L\alpha}\left[P_0\left(\frac{\lambda_0}{d}\right)^\beta - \frac{2\gamma}{R_p}\right]\right\}.$$

(17)

10

CHAPTER III

METHODS

3.1. Modeling Pore Geometry

In *Rempel* (2012), a similar study was performed in two-dimensions. We chose to adapt the problem to three dimensions because the pore geometry of three-dimensional sedimentary packing differs from two-dimensional pore geometry in two distinct ways. First, the pore itself is three-dimensional, therefore surfaces within three-dimensional pore have two principle radii of curvature rather than just one. Second, a difference in geometry arises from off-plane particle contacts in three-dimensional packing. We model three-dimensional pore geometry by simulating a sphere packing process in MATLAB (described in further detail in the appendix). To describe the geometry of the particle spheres that are being "packed," the model accepts as inputs a number of particles n, and either a Gaussian distribution with a mean radius r_{mean}, and standard deviation σ, or some other particle size distribution. This allows pore geometry to be simulated for a desired set of particles both when only an average value for the particle radii is available, as shown in *Section 4.2-4.4*, and when an exact probability distribution for particle radii is available, as shown in **Section 5**.

Once the packing process is complete, the three-dimensional pore geometry is available for evaluating the equilibrium phase perturbations. We implement a Monte Carlo integration routine in which the phase behavior is evaluated at a large number of randomly selected test points. If a given test point lands within a particle, the model

records the event for a porosity calculation. If the test point falls within the pore space,

we use the location of the test point and the geometrical constraints imposed by the

nearest particles for a series of calculations to predict the magnitude of undercooling at

which hydrate first encompasses that point. After the data are compiled, the residual

liquid saturation is determined as the ratio of the number of test points that are outside the

non-wetting phase at a particular undercooling relative to the total number of test points

contained within the pore space.

3.2. Three-Dimensional Calculations

3.2.1. Pore Hydrate

As the temperature begins to drop below freezing, the curvature of the hydrate is

primarily responsible for the undercooling, as illustrated in **Fig. 2**. We calculate the

largest sphere that can fit in the pore and still contain the test point, and refer to the

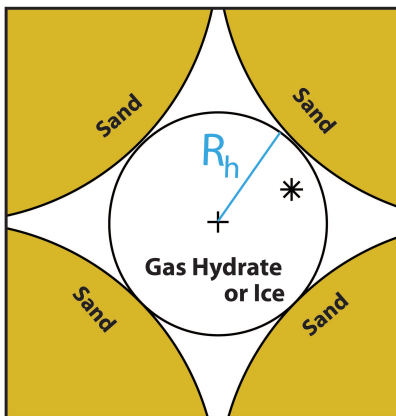resulting undercooling as the "pore hydrate" value.

Fig. 2. Simplification of pore hydrate geometry. The diagram shows how we use the location of a test point to find the radius R_h, of curvature for a pore hydrate. The asterisk is an example of a test point randomly chosen in a packing of spherical sedimentary or "sand" particles.

This process begins by first putting a sphere in the pore with the test point as the center and a radius that is equal to the distance between the test point and the nearest particle. Then we grow the sphere by incrementally moving its center point and changing its radius to match the new distance to its nearest neighbor. If the pore geometry does not permit a particular move or if the radius decreases, the model retains the previous size and location of the hydrate sphere. When the model reaches a set number of iterations, the radius is saved as the radius of the pore hydrate crystal R_h. The undercooling that would be required to place the point within this approximation for the largest hydrate crystal that could nucleate within the pore is found by combining equations (10) and (12) to obtain

$$T_m - T \approx \frac{T_m}{\rho_h L} \frac{2\gamma_{hl}}{R_h}. \tag{18}$$

3.2.2. Crevice Hydrate

After hydrate forms within a pore, the hydrate will continue to grow with a non-planar geometry, as seen in **Fig. 1D** and **Fig. 3**. We simulate the curvature of the "crevice hydrate" by finding the radius of the largest sphere that is tangent to the test point and the two particle spheres that are closest to the test point. The process to find this radius involves several steps. First, the test point and the center points of the two nearest spheres are rotated into the same two-dimensional plane to solve for the radius of the largest tangent circle. The two nearest circles now have center points (x_1, y_1) and (x_2, y_2) and radii of r_1 and r_2, while (x_3, y_3) describes the location of the test point, with a radius of $r_3 = 0$. Apollonius, a Greek geometer from the 3rd century BC (Cantarella et al., 2002),

13

showed that given three initial circles, a total of eight tangent circles exists. However, by reducing one of the three initial circles to a point, the number of solution circles reduces to two. The solution circles are tangent to the two initial circles and the two solution circles are tangent to the initial circle that has been reduced to a point. Because we want to solve for a tangent solution circle that does not intersect the two original circles, there exists only one solution circle with a center at (x, y) and a radius r. We calculate the solution by first using the equation of a circle to produce six quadratic equations, where $i = 1{:}3$, using

$$(x - x_i)^2 + (y - y_i)^2 - (r \pm r_i)^2 = 0. \tag{19}$$

Which can be expanded to six equations described by the following equation,

$$(x^2 + y^2 - r^2) - 2xx_i - 2yy_i \mp 2rr_i + (x_i^2 + y_i^2 - r_i^2) = 0. \tag{20}$$

Then by subtracting equation (20) with $i = 2$ from the version with $i = 1$ and again with $i = 3$ from $i = 1$ we obtain

$$ax + by + cr = d \tag{21}$$

and

$$a'x + b'y + c'r = d' \tag{22}$$

where

$$a = 2(x_1 - x_2), \quad a' = 2(x_1 - x_3), \tag{23 - 24}$$

$$b = 2(y_1 - y_2), \quad b' = 2(y_1 - y_3), \tag{25 - 26}$$

$$c = \pm r_1 \pm r_2, \quad c' = \pm r_1 \pm r_3, \tag{27}$$

$$d = (x_1^2 + y_1^2 - r_1^2) - (x_2^2 + y_2^2 - r_2^2), \tag{28}$$

and

$$d' = (x_1^2 + y_1^2 - r_1^2) - (x_3^2 + y_3^2 - r_3^2). \tag{29}$$

The equations above can then be substituted back into equation (19) and solved using the quadratic formula. For our purposes, the equations are simplified because $r_3 = 0$. Once we find the two Apollonius circles, the circles that are tangent to the test point and the two nearest circles, we can narrow down our solutions to the only circle that meets our requirements. Now we know the positive radius of curvature for the crevice hydrate, R_{h1}. However, the crevice hydrate is not necessarily spherical, but can grow around the crevice in the third dimension. We also account for the negative radius of curvature R_{h2} for the hydrate growing in the crevice points as illustrated in **Fig. 3**.
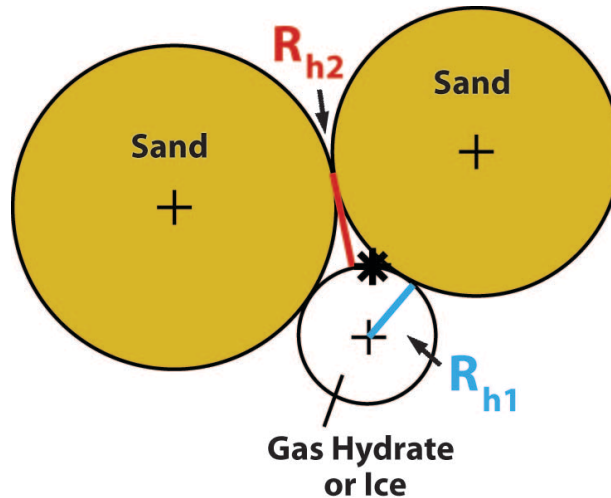

Fig. 3. Simplification of crevice hydrate geometry. The diagram shows how we use a test point to find the positive and negative radii of curvature for a crevice hydrate, R_{h1} and R_{h2} respectively. The asterisk is an example of a test point randomly chosen in a packing of spherical sedimentary or "sand" particles.

Finally, we can calculate what perturbation to the chemical potential would be required to place the point within a crevice between particles with a constant curvature hydrate-liquid interface using

$$T_m - T \approx \frac{T_m \gamma_{hl}}{\rho_h L} \left[\frac{1}{R_{h1}} - \frac{1}{R_{h2}} \right]. \tag{30}$$

3.2.3. Wetting Film

After hydrate saturates nearly all of the pore space, the particles are still coated by thin liquid films (**Fig. 4**).
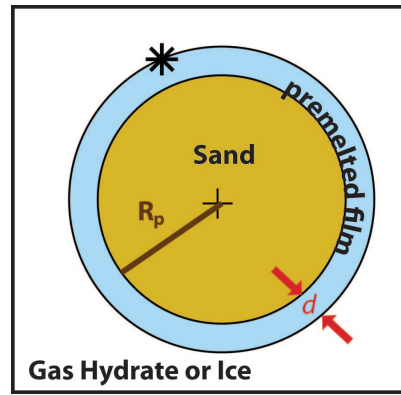

Fig. 4. Simplification of liquid film geometry. The diagram shows how we use a test point to find the radius of curvature for a particle sphere nearest to the test point for the film undercooling calculation. The asterisk is an example of a test point randomly chosen in a packing of spherical sedimentary or "sand" particles.

We use the distance of the point from the particle d and the radius of the particle R_p to calculate the undercooling that would be required to place the point on the edge of a wetting film as

$$T_m - T \approx \frac{T_m}{\rho_h L} \left[P_0 \left(\frac{\lambda}{d} \right)^\beta - \frac{2\gamma_{hl}}{R_p} \right]. \tag{31}$$

16

Equation (31) is essentially equation (16), with a more specific application to the hydrate-liquid system. The precise nature of the wetting interactions that produce liquid films depends on the surface chemistry and is the least well-constrained portion of our calculations. There exists a range of potential wetting interactions with different functional dependencies between undercooling and film thickness. To provide flexibility, we have produced a follow-up code that uses the geometrical output (i.e. R_{h1}, R_{h2}, d...) of the original model, but allows us to adjust any parameter, and the entire film thickness parameterization to test their effects.

3.3. Model Output

Equations (18), (30), and (31) yield estimates for the undercooling that is expected of "pore hydrate," "crevice hydrate," and "film hydrate." We use the largest of these perturbations to the melting temperature at each test point to determine the undercooling at that particular location. Once this process is completed for all of the desired test points, we can calculate the undercooling versus liquid saturation for the system. Here, the liquid saturation is defined as the fractional volume of the pore space that is occupied by liquid. Our model produces two total undercooling curves, which differ slightly in their treatments of "crevice hydrate". In **Section 4** and **Section 5** we use both of the total curves from **Fig. 5**, which we refer to as the "crevice curve" and the "pore curve", to fully test our model against analytical approximations and measured undercooling data. Later we show that the pore curve (Fig. 5A) is more valid at higher liquid saturations and the crevice curve (Fig. 5B) becomes more valid at lower liquid saturations.
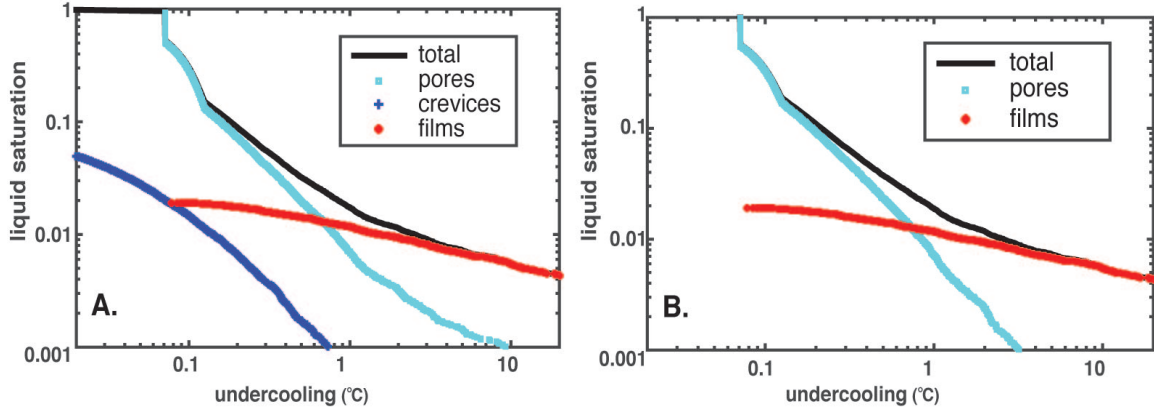
Fig. 5. An example of model prediction results. The black curves show the total predicted undercooling ΔT for a unit cube of simple-cubic packing with a radius, $r_{unit} = 1\mu m$. The portion of the total undercooling the model attributes to pore hydrate geometry is plotted in cyan. The portion of the total undercooling the model attributes to crevice hydrate geometry is plotted in blue. The portion of the total undercooling that is caused the presence of thin liquid films is plotted in red. (A) Shows the undercooling curve that is influenced by the crevice hydrate points. Later we show that this curve, the crevice curve, becomes more valid at lower liquid saturations than (B). (B) Shows the undercooling curve that we refer to as the pore curve, which is not influenced by crevice hydrate points. Later we show that this curve is more valid at higher liquid saturations than the crevice curve.

For the crevice curve, we omit the pore hydrate calculation for test points that are in positions likely to be incorporated within crevice hydrates with two oppositely signed radii of curvature. This is judged by comparing the "particle-circle angle" subtended by line segments connecting the center of the Apollonius circle to the tangencies on two nearest particle spheres, to the maximum angle subtended by the line segments connecting the test point with the center of the Apollonius circle and each of the two tangencies. If this maximum angle is less than the "particle-circle angle," then the point is a candidate crevice point and we do not perform the pore-hydrate calculation for this point when we generate the crevice curve. In the second case, which we refer to as the pore curve, we omit this filtering step and treat each point as though it might fall on a hemispherical hydrate cap. Unfortunately, which of these two cases better represents the

hydrate geometry at a particle test point depends on hydrate occupancy in adjacent pores and is not easily diagnosed by our numerical treatment. Nonetheless, we expect that the true saturation behavior will be somewhere between these limiting cases, and our calculations demonstrate that both sets of model saturation curves are similar (**Fig. 5**).

The particle size distributions of the spheres we pack drastically affects the degree of undercooling i.e. the more fine-grained the particles, the more dramatic the undercooling or disturbance to the phase equilibrium. To illustrate this point, in **Fig. 6** we plotted the undercooling curves for packed sphere models that have different mean radii r_{mean}, and standard deviation $\sigma = \frac{r_{mean}}{100}$. Notice that the slopes of the undercooling curves in log space begin to become more gradual at lower liquid saturations for the more fine-grained sphere packings; this is due to the increasing influence of the thin liquid films that coat the particles.
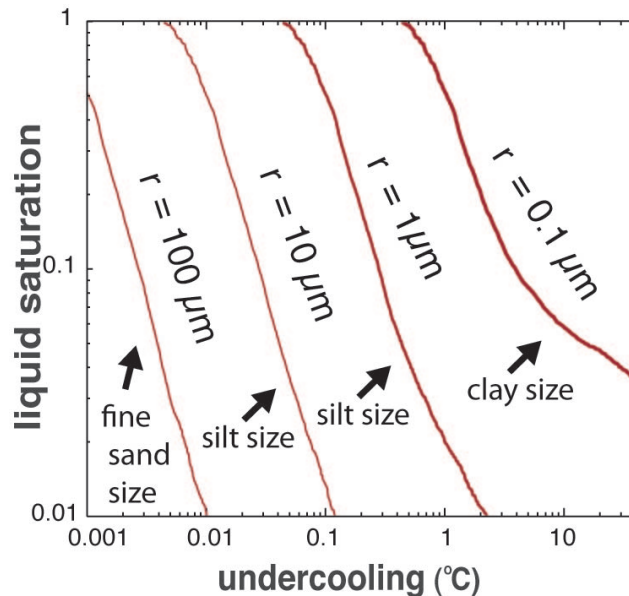

Fig. 6. Particle size versus undercooling. This graph illustrates the change in undercooling magnitudes that accompany a change in mean radius, the smaller the mean radius, the larger the undercooling for a given liquid saturation. The mean radius is labeled as r on the graph. We only plot the pore total curve associated with each sphere packing to simplify the plot.

19

CHAPTER IV

MODEL VALIDATION

We test our model in several different ways. The input parameters used by our model are described in **Table 1**.

Table 1. Model input parameters for the calculations that are discussed below.

	Idealized Packing	Ice-liquid	Ice-liquid	Liquid Vapor
Composition of porous medium	None – computationally modeled sphere[1]	Polystyrene powder[1]	Graphitized carbon black powder[1]	Millville Silt Loam[2]
r_{mean} (μm) mean radius	1[1]	2.5[1]	0.1075[1]	17.1[2]
σ (μm) standard deviation	0[1]	0.16*	0.0625[1]	0.385*
T_m (K) reference temperature	273[1]	273[1]	273[1]	273[1]
$\rho \left(\dfrac{kg}{m^3}\right)$ density non-wetting phase	917[1]	917[1]	917[1]	NA
$\gamma \left(\dfrac{J}{m^2}\right)$ interfacial surface energy	0.029[1]	0.029[1]	0.029[1]	0.073[3]
$L \left(\dfrac{J}{kg}\right)$ latent heat	917[1]	917[1]	917[1]	NA
λ_0 (μm) film thickness at p_0	3.5e-9[1]	3.5e-9[1]	3.5e-9[1]	1.6e-6
p_0 (Pa) scale for disjoining pressure	1.1e6[1]	1.1e6[1]	1.1e6[1]	1.1e6[1]
β power-law exponent for film thickness	3[1]	3[1]	3[1]	3[1]

NA is not applicable
[1]Source is *Cahn et al.* (1992)
[2]Estimated using values provided in *Or and Tuller* (1999)
[3]Source is *Vargaftik et al.,* (1993)
*Not provided, so we used $\sigma = \sqrt{r_{mean}}/100.$

First we compare it against idealized simple-cubic (SC) sphere packing with an undercooling curve that has several attributes that are easily calculated analytically. Then we use our model to compare the model predicted undercooling against laboratory-measured values for two ice-liquid systems. Finally, we test our model by comparing the change in matric potential versus liquid saturation for a liquid-vapor system.

4.1. Comparison to Analytical Approximation

We compare our undercooling predictions for idealized SC packing against an analytic approximation for idealized SC packing (**Fig. 7**).
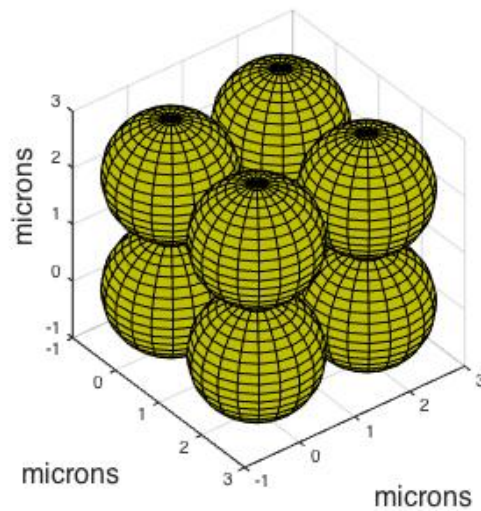

Fig. 7. An example of simple-cubic packing of spheres with radii $r_{sc} = 1\mu m$ shown at an oblique angle.

Cahn et al. 1992 use the geometry of SC sphere packing to predict the evolution of ice formation as a function of undercooling within an idealized pore space. They develop theoretical equations for the undercooling of ice freezing in SC sphere packing for any given radius that we refer to as, r_{sc} (Cahn et al., 1992). We modify the equations

21

used to develop their theoretical curve to match only the undercooling effects that we account for in this study, by neglecting grain-boundary effects that are sensitive to unknown crystallinity.

In **Fig. 8** we illustrate some important features of the undercooling predictions produced by our model. Notice that the pore total curve, that is not influenced by crevice solids, does a better job matching the expected behavior from a liquid saturation of 1 to about 0.35 than the crevice total curve. This suggests that the pore total undercooling curve is more accurate at warmer temperatures than the crevice total curve. The crevice total curve does a better job matching the expected behavior starting around a liquid saturation of 0.1 and below. This suggests that while erroneous at warmer temperatures, the crevice total undercooling curve becomes more accurate as the temperature continues to drop and the liquid saturation decreases. Further calculations suggest neither of the model predicted curves accurately captures the undercooling between the liquid saturations of about 0.35 to about 0.1 for SC sphere packing. However, the similarity between the two models and the analytical approximation suggests that the resulting errors in predicted saturation are likely small.

We expect this difference between the pore and crevice undercooling curves because the pore filling process dominates as solid first begins to fill the pore space, and becomes less substantial as the solid continues to fill the pore space and the temperature decreases (**Fig. 1**). Both of the model predicted undercooling curves converge as the temperature continues to drop and wetting interactions between the solid, liquid, and particles begin to dominate over curvature effects. We use both curves in our model comparisons against laboratory data in *Section 4.2*.
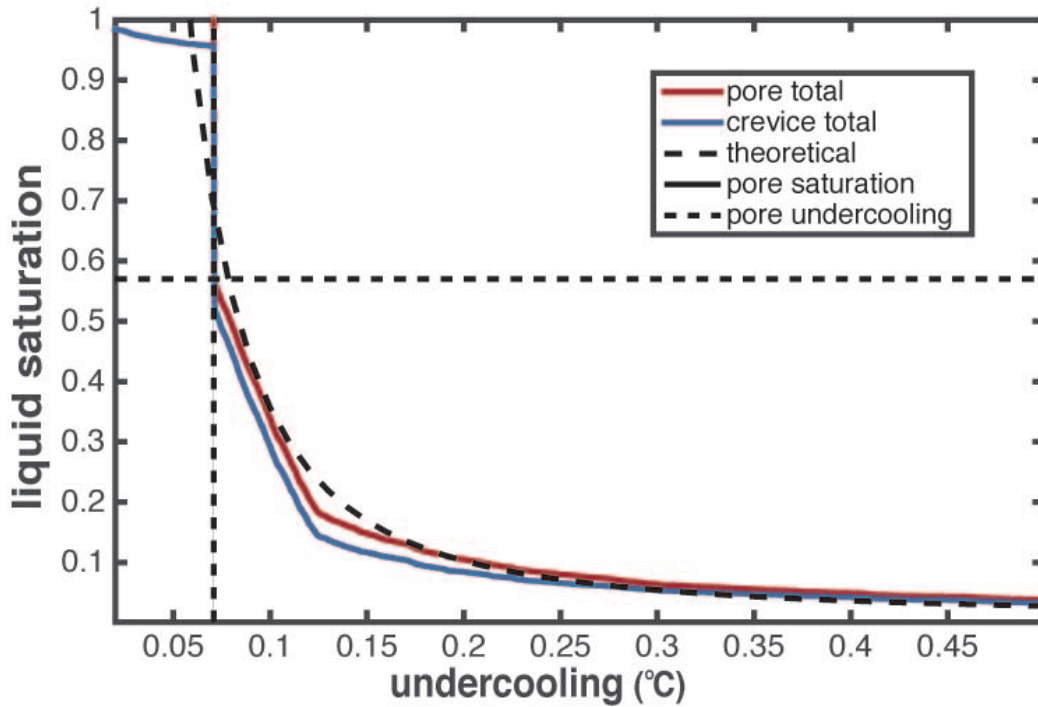
Fig. 8. Model predicted undercoolings versus analytical approximations. The figure contains both the model predicted pore total undercooling curve, shown in red, and the model predicted crevice total undercooling curve, shown in blue. The black dashed curve is the analytical approximation from *Cahn et al.* (1992) that approximates the undercooling based on the geometry of SC sphere packing with a radius of $r_{sc} = 1\mu m$ accounting for crevice and film points, but not the pore hydrate points included in this study. The dashed straight lines intersect at the first kink in our model's curves. This kink occurs at a liquid saturation of 0.57, and undercooling 0.078 °C, that correlate to the central pore being filled by the largest sphere that can occupy the void space. The pore total curve captures this feature, but the crevice total curve allows hydrate formation at warmer temperatures than are possible, a limitation also shared by the *Cahn et al.* (1992) approximation.

4.2. Ice-water Comparisons

After the successful comparison between our model predictions and anticipated

behavior in simple-cubic packing, we compare our model results to laboratory data as

shown in **Fig. 9**. We use two undercooling datasets from *Cahn et al.* (1992) for a two-

phase ice-water system within a medium composed of monosized spheres composed of

polystyrene powder and graphitized carbon black. First we compare our model results against the measured undercooling values for the graphitized carbon black (**Fig. 9A**).

When comparing our model's undercooling predictions against the undercooling data for graphitized carbon black powder, **Fig. 9A**, both curves fit entirety of the dataset well. However, at saturations above approximately 10%, the pore total slightly overestimates the undercooling liquid. This is not surprising because the pore total curve should account for an excess of curvature effects, leading to slightly over-predicted undercooling values.
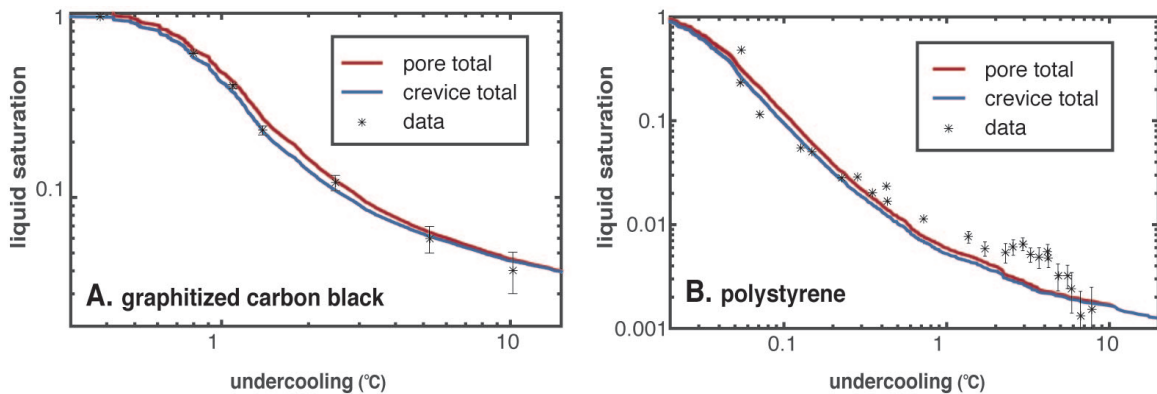

Fig. 9. Model predicted undercooling versus undercooling data from ice melting laboratory experiments. The red curves in both plots represent the undercooling curves that are dominated solely by pore hydrates until the liquid saturation is sufficiently low for the wetting effects to govern. The blue curves in both plots represent the undercooling curves that are influenced by crevice hydrates. Notice that the axes are slightly different between the plots, optimized for the data that each is displaying. (A) Comparison of our model's undercooling predictions against undercooling data for ice melting in mono-dispersed graphitized carbon black powder shown in black asterisks (Cahn et al., 1992). The R-squared values for the pore and crevice curves in (A) are 99.35% and 99.75%, respectively. (B) Comparison of our model's undercooling against undercooling data for ice melting in mono-dispersed polystyrene powder shown in black asterisks (Cahn et al., 1992). The R-squared values for the pore and crevice curves in (B) are 82.33% and 79.25% respectively.

When comparing our model's undercooling predictions against the undercooling data for the polystyrene powder, both curves mimic the general trend of the data, but the model does not do nearly as good of a job predicting the undercooling in **Fig. 9B** as it does for graphitized carbon black in **Fig. 9A**. However, notice that in **Fig. 9A**, only two

of the data points fall below 10% liquid saturation. In **Fig. 9B**, the majority of the data

occurs between 10% and 0.1% liquid saturation. At such low liquid saturations, wetting

effects are responsible for most of the residual liquid. The detailed nature of the

intermolecular forces that cause pre-melted films to form is the least well-constrained

part of our calculation. In fact, because wetting effects are dependent on particle

composition and surface chemistry, we expect some variance in the undercooling effects

between the two systems depicted in **Fig. 9A** and **Fig. 9B**. Due to the complicated nature

of the pre-melted films, we developed our model to output the predicted undercooling

data as well as geometrical information we compiled for pore characteristics that could

affect hydrate growth at each test point. This allows us to run quick simulations where we

can recalculate the undercooling curve for the same pore geometry but with desired

adjustments in the reference film thickness λ_0, the power-law exponent β, or any of the

other input parameters. This is useful for undercooling values such as those shown in **Fig.
9B**, where several of the data points occur where the liquid saturation is between 1% and

0.1% and the behavior of pre-melted films can become increasingly complex (Cahn et al.

1992).

4.3. Liquid-vapor comparison

The adsorption of water to sedimentary particles in a liquid-gas system occurs in

the vadose zone. This important effect is essential for plants to obtain water in

unsaturated soil, and is a consequence of the same forces that cause undercooling in ice-

liquid systems. We compare our model prediction for the matric potential of Millville

silt-loam against experimental results (Or and Hanks, 1992; Or and Tuller, 1999; Tuller and Or, 2005) in **Fig. 10**.
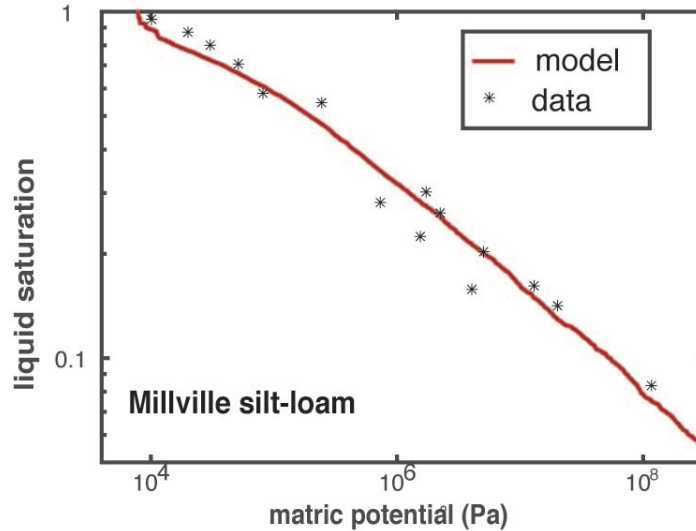

Fig. 10. Model predicted matric potential curve versus matric potential data. This plot displays the comparison of our model's prediction plotted as a red curve to data from *Or and Hanks's (*1992) laboratory experiments plotted as black asterisks. Notice that the slope of the curve is more gradual than those in **Fig. 9**. This shallow slope of the matric potential curve for this dataset suggests that wetting effects are dominating the system. To match the data we require strong intermolecular forces, so we increase λ_0 in comparison with the previously used values (**Table 1**). Because wetting effects dominate, the pore total curve and the crevice total curve are nearly identical and we only plot the pore total curve. The model predicted curve accurately predicts the matric potential required for the saturation to begin decreasing. The R-squared value for our matric potential curve is 96.84%.

The λ_0 parameter, which scales the film thickness, needed to match the data was nearly three orders of magnitude larger than the λ_0 used for the ice-liquid experiments (**Table 1**). It is not entirely unexpected that the Millville silt-loam sediments might produce stronger wetting effects than the powders used in *Section 4.2*. The most obvious difference is that natural soil was used by *Or and Hanks (*1992). The intermolecular forces active in natural soil may cause wetting effects to be stronger or weaker than in

26

laboratory prepared monosized powders (Saarenketo, 1998). The Millville silt-loam sediments are composed of a broad range of particle sizes: 33% sand, 49% silt, and 18% clay (Or and Tuller, 1999). To estimate the mean radius r_{mean}, we used estimates on the finer side of their particle size classifications for each grain size, where radius of sand particles = $50\mu m$, radius of silt particles = $1\ \mu m$, and radius of clay particles = $0.5\ \mu m$. Because loam is composed partly of clay, the surface wetting interactions are likely even more complex (Oss and Giese, 1995). The presence of clay in the Millville silt loam presents another issue, inherent to the sphere-packing model design: non-spherical particles. The presence of non-spherical particles likely has a dramatic effect on the ability of our code to model the pore geometry accurately, thereby affecting our ability to predict disturbances to the chemical potential caused by the pore geometry. If the average of the specific surface areas ($76.5 m^2/g$) reported in *Or and Tuller* (2005) for the Millville silt loam is used to calculate a spherical particle radius using a silica density of $2.65g/cm^3$, the corresponding radius should be about $0.015\ \mu m$, which is about three orders magnitude smaller than our estimated radius shown in the table at $17.1\ \mu m$. As the size of spherical particles decrease, their specific surface area increases linearly; the relationship between clay particles and specific surface area is not as simple. However, by simply increasing λ_0 we have been able to produce model results that well approximate the data.

CHAPTER V

HYDRATE MODEL

Our model is designed so that particle size distributions from adjacent layers can be used to predict the phase behavior that leads to the growth of hydrate anomalies. The particle size distribution data allow us to predict the equilibrium concentration difference between adjacent sedimentary layers. This is important because the methane concentration at layer boundaries is tied to the equilibrium concentration in the coarser material in which hydrate precipitates, as illustrated in **Fig. 11** (Clennell et al., 1999; Cook and Malinverno, 2013; Daigle and Dugan, 2011; Rempel, 2011).
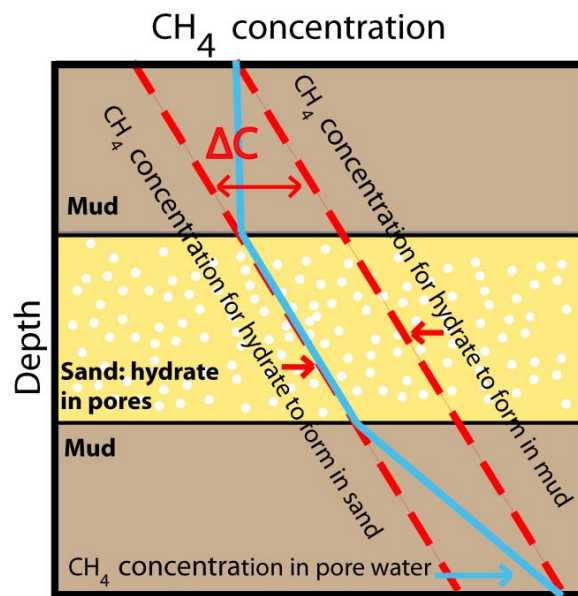

Fig. 11. Layer boundary effects on methane concentration, modified from **Figure 4** in *Cook and Malinverno 2013*. This diagram illustrates that although there is a jump in equilibrium concentration of methane between the mud and the sand (red dashed lines), the concentration of methane within the pore water cannot abruptly change (light blue line). Therefore, in the locations where the mud is directly adjacent to the hydrate-bearing sand, methane hydrate is absent in the mud (Cook and Malinverno; 2013).

To demonstrate how our model could be used to predict hydrate anomalies using particle size distributions, we use borehole data collected during the Indian National Gas Hydrate Program Expedition 1 (NGHP-01) at site 17A in the Andaman accretionary wedge (Collett et al., 2008; Rose et al., 2014). Here, thin (~10 cm), coarser-grained ash layers punctuate the stratigraphic record, which is otherwise dominated by pelagic sediments (Rose et al., 2014). These ash layers contain anomalous accumulations of hydrate, in many cases filling more than 70% of the ash pore-space (Rose et al., 2014). Such hydrate saturation anomalies may be the result of diffusive methane flux from finer-grained sediments into coarser-grained layers (Cook and Malinverno, 2013; Malinverno and Goldberg, 2015; Rempel, 2011). Using our model, we predict undercooling values for the ash and pelagic sediment layers at NGHP-01 site 17A given particle size distributions for each layer from *Rose et al.* (2014).

First, we use the plot from **Figure 3** from *Rose et al.,* (2014) describing the ash layer and the surrounding bulk sediments from core 51X to calculate the probability distribution functions (PDFs) for the particle radii. We use these PDFs to create two sets of randomly ordered spheres (**Fig. 12**).
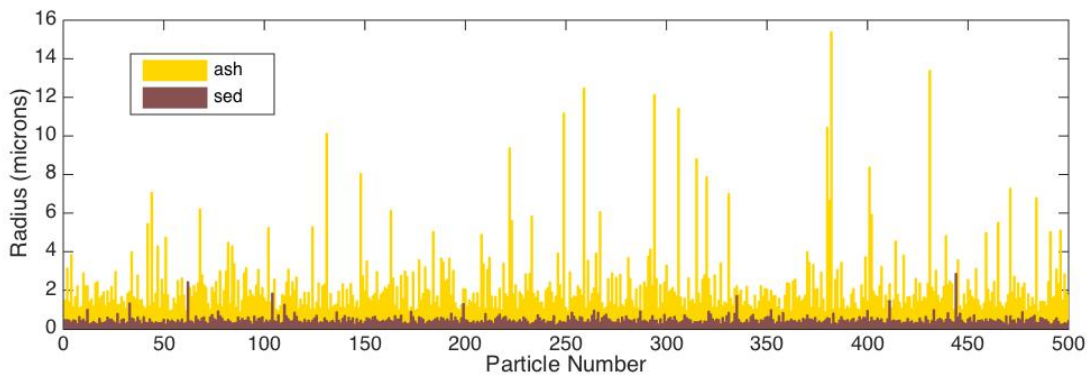

Fig. 12. Randomized radii distribution for the first 500 particles for layers created by using the data from **Figure 3** in *Rose et al., 2014*. Notice that the ash particles are substantially coarser than the bulk sediments that encompass the ash layer.

29

Once the datasets describing the particle sizes have been randomized, we were able to pack the spheres and mimic the pore space geometry of the ash and surrounding bulk sedimentary layers (**Appendix A**). We use the methods outlined in **Section 3** to predict the undercooling for each of the datasets (**Fig. 13**).
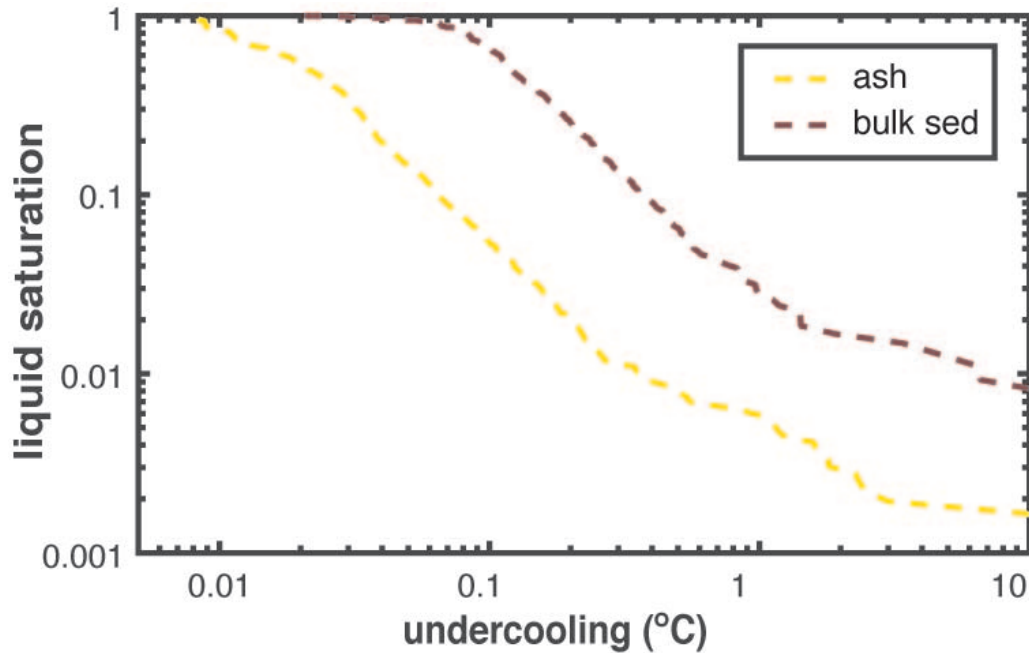

Fig. 13. Undercooling curves for hydrate model. This plot shows that as hydrate forms and the liquid saturation reduces, the undercooling caused by the pore geometry and interactions with the particles more dramatically affects the finer grained sediments relative to the coarser ash layers. This implies that at the same subzero temperature, more hydrate will be frozen in the coarser ash layer than in the more fine-grained sedimentary deposits layer.

However, for hydrate anomalies, we are interested in how porous media affect the solubility of methane in aqueous solution adjacent to the hydrate within each layer. By utilizing equation (17), we convert the undercooling caused by the porous medium to the change in equilibrium concentration relative to the bulk equilibrium concentration (**Fig. 14**).
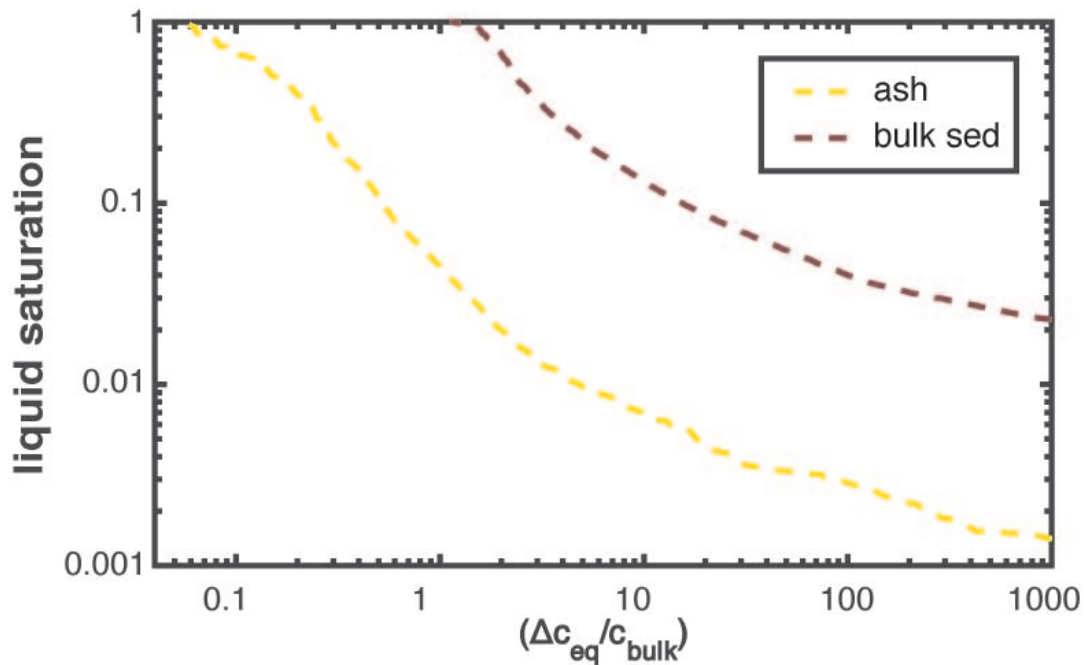
Fig. 14. Relative porous medium effects on equilibrium concentration. This plot shows that the difference in equilibrium concentration required for hydrate freezing within a porous medium is greater in the more fine-grained sedimentary layer. This difference in equilibrium concentrations causes methane hydrate solubility differences between the adjacent layers that are ultimately the cause of hydrate anomalies. Because the altered equilibrium concentration in the more fine-grained sedimentary layer is higher than in the ash layer, hydrate is slightly more stable in the coarser ash layer (Cook and Malinverno, 2013; Rempel, 2011; Malinverno and Goldberg, 2015). Therefore, the higher concentration of methane required for hydrate to form in the adjacent fine-grained deposits cannot be achieved until sufficiently high hydrate saturation (corresponding with a liquid saturation of a few percent in this figure) is reached in the ash layer.

The difference in solubility between the adjacent layers is an important factor when considering hydrate anomaly formation (Rempel, 2011). By using our tools described in this paper, we can predict this difference in solubility. In **Fig. 15** we show the results of a model that used our model's results as input along with parameters provided in *Rose et al.,* (2014) to predict the saturation of methane hydrate growing within the ash layer sandwiched between more fine-grained sediments.
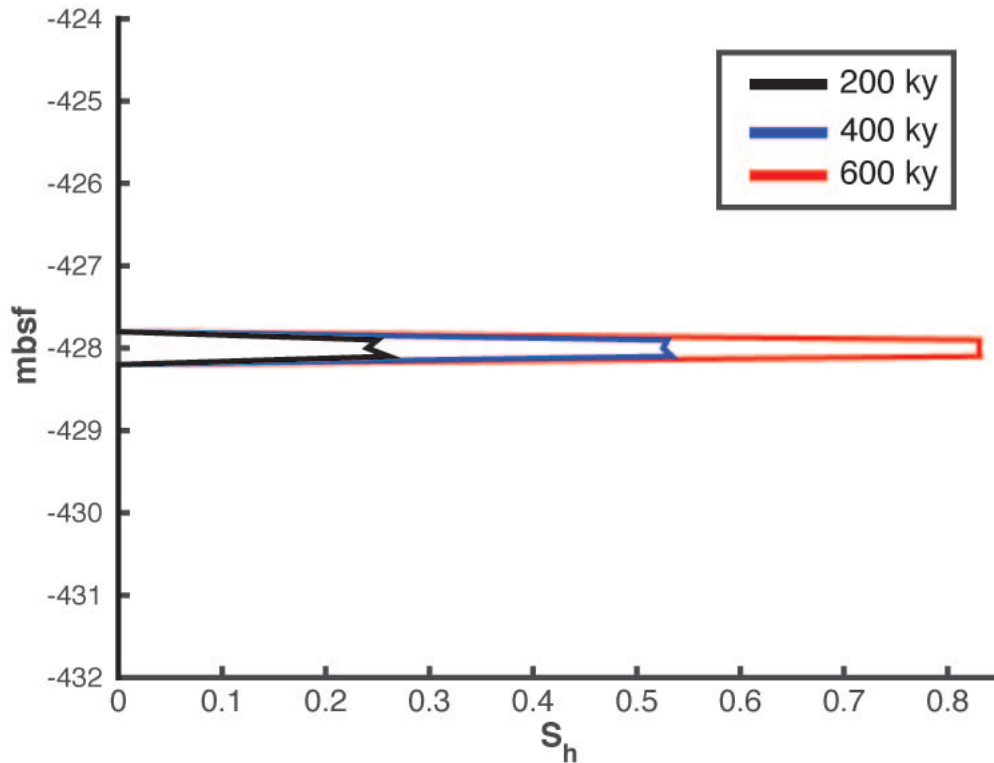
31

Fig. 15. Hydrate saturation over time. This plot shows the hydrate saturation S_h versus meters below seafloor (mbsf) predicted using parameters from *Rose, et al.* (2014) and the model predicted differences in undercooling. The model predicted hydrate saturation of the anomaly is 80.7% and measured hydrate saturation of the anomaly is 83%. The different colored lines correspond to how long the hydrate was allowed to accumulate in the model. This figure was provided by Brandon VanderBeek.

Following the 1D formulation of *Rempel* (2011), we use the predicted undercooling curves from the model to predict the diffusive growth of hydrate within a horizontal, 10 cm thick ash layer at 428 meters below the seafloor (Rose et al., 2014). For modeling simplicity, we approximate the dependence of undercooling on hydrate saturation as a power-law relationship and find the best-fit exponent ($\beta = 1.35$) to the undercooling curves in **Fig. 13** for liquid saturations between 0.02 and 0.75. This approach is valid as we are interested in hydrate saturations well below 98%. We assume dissolved methane is supplied from below at an upward fluid transport rate of 0.5 mm/a,

a rate representative of the region (Dewangan et al., 2011) and the pore water methane

concentration is initially at equilibrium. Additional site-specific information required to

model hydrate accumulation includes water depth (1344 m), seafloor temperature (5.5

°C), geothermal gradient (0.021 °C /m), and depth to the base of the gas-hydrate stability

zone (605 mbsf) are taken from *Rose et al.* (2014). We find hydrate saturations reach

83% within the thin ash layer at 600 ka (**Fig. 15**). The sediment surrounding the ash layer

contains <1% hydrate. These results compare well with borehole measurements at

NGHP-01 site 17A, where a 9.5 cm thick ash layer at 428 mbsf was found to contain

81% hydrate (Rose et al. 2014). However, because the age of the hydrate deposit is

unknown, similar hydrate saturations can be produced for a range of undercooling values.

Nonetheless, pore-scale effects control the size and distribution of hydrate anomalies and

will continue to prove useful when characterizing hydrate reservoirs.

CHAPTER VI

CONCLUSION

As we continue to increase our understanding of the nature and distribution of gas hydrates, we become more aware of the importance of gas hydrate anomalies. In an effort to help predict the occurrence and saturation of gas hydrate anomalies, we focus our efforts on understanding the pore-scale effects that are likely to be the cause of the gas hydrate anomalies (Rempel, 2011; Rose et al., 2014). The differences in sedimentary properties, particularly grain size, between adjacent sedimentary layers produce small differences in the equilibrium concentrations. These small differences are likely the cause of gas hydrate anomalies that compose most of the volume of gas hydrate off the continental shelf (Clennell et al., 1999; Cook and Malinverno, 2013; Daigle and Dugan, 2011; Rempel, 2011). We demonstrate that our tool closely approximates the chemical disturbance to the equilibrium within porous media that have mostly spherical particles. The shortcoming of our model is that the model less effectively captures the pore geometries of sedimentary layers that contain non-equant particles and the associated increase in the strength of the wetting interactions for these layers. The increase in the strength of the wetting interactions is likely due to the increase in specific surface area of clay particles. Improvements can be made in the future to try to account for the presence of non-spherical particles. Fortunately, as our comparison in *Section 4.3* demonstrates, these interactions may be accounted for by increasing the reference film thickness λ_0. These predictions are the first step to developing reliable quantified estimations of hydrate anomaly reservoirs and saturations.

APPENDIX

MODELING A 3D POROUS MEDIUM

We created a tool that simulates a sphere packing process in MATLAB to use the curvature of the spheres and the void space geometry between the spheres as a way to model the pore space geometry of naturally accumulated sediments. As stated in *Section 3.1*, the model can run given inputs as straightforward as the number of desired particles n, a mean radius value r_{mean}, and standard deviation σ. However, the tool can also create a data set for a set of n particles from a particle size distribution curve, or even from a volume percent versus radius curve; the latter was developed for the specific application addressed in **Section 5**. We cover the steps for the sphere packing process started by inputting a particle size distribution to determine the distribution of particle radii (**Fig. 16**), as the overall sphere packing process is the same regardless of the chosen input.
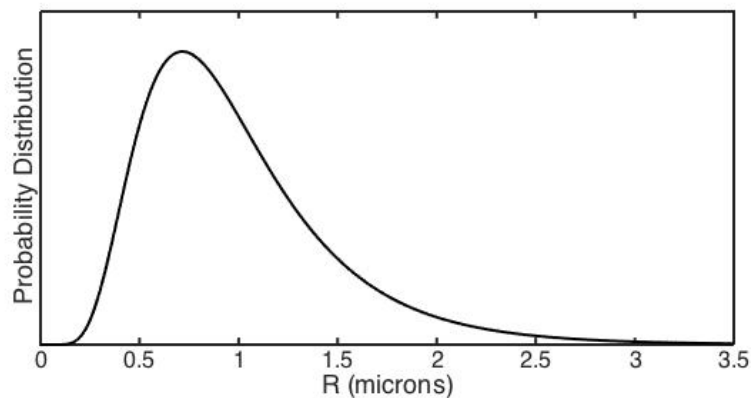

Fig. 16. A Gaussian probability distribuion function (PDF) in microns for the radii of a set of particle spheres. This particular PDF describes a set of particles with $r_{mean} = 1\mu m$ and $\sigma = 0.5\mu m$ for a set of $n = 1000$ particles.

To create a set of particles whose radii satisfy the PDF in **Fig. 16**, we must sum

the probabilities for each radius of the PDF to calculate the corresponding cumulative

distribution function (CDF) as shown in **Fig. 17**. We can then split the CDF into n equal

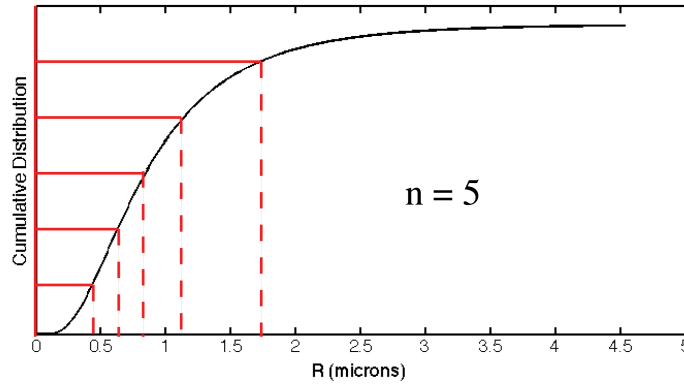intervals, each n division corresponds to a particle radius r

Fig. 17. The segmentation of a cumulative distribution function to create a dataset
containing particles with radii that satisfy a corresponding PDF. Here, n is chosen to be 5
for the purpose of illustrating the process used to choose the radii. The solid red lines
show equally spaced probability of n intervals. For each probability interval, there is a
corresponding radius, illustrated by the dashed red lines. For n intervals we determine
n radii.

After the CDF has been used to choose n particle radii, we have a synthetic data

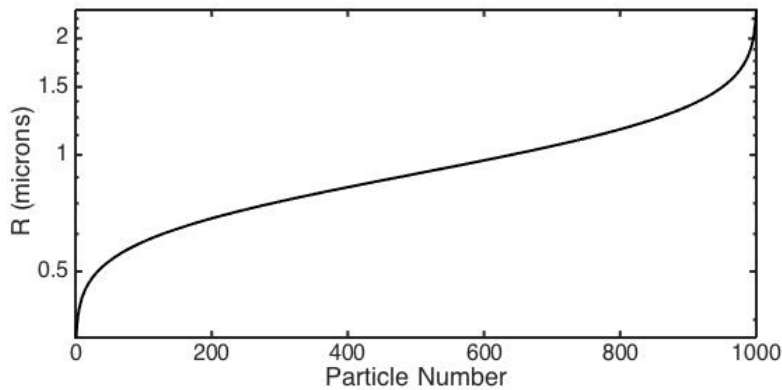set that describes the radii of n particles (**Fig. 18**).

Fig. 18. Particle spheres with their corresponding radii. In this plot $n = 1000$.

36

Once a set of n particles has been developed that satisfy the desired PDF, our next step is to randomize the order of the particles (**Fig. 19**). We randomize the particle order because our sphere packing process involves dropping the particle spheres one by one and the goal is to create a pore geometry with natural characteristics.
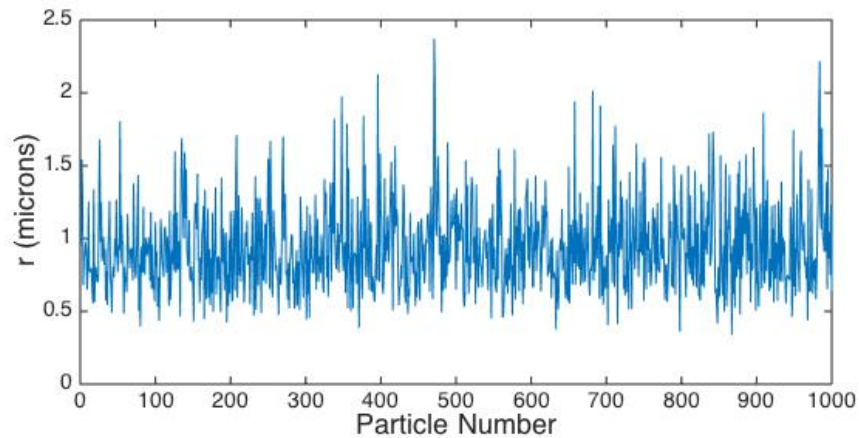

Fig. 19. Randomized particle spheres and their corresponding radii. In this plot $n = 1000$.

Once the dataset containing the randomized particle spheres is complete, we can begin the sphere dropping process. The process works by dropping each particle sphere one at a time. We simulate the dropping process by first choosing an arbitrarily high z-coordinate. Then the x-y coordinates at which each particle sphere is dropped is chosen by first defining lengths of a "container" and randomly choosing x-y coordinates within the specified x-y container space. The particle sphere is then "dropped" down the z-axis with the corresponding x-y coordinates. We mimic this process by checking the x-y position of all of the previously dropped spheres to see if the dropping sphere and the previous spheres would overlap. If there are no previously dropped spheres within this "window," then the particle sphere will make contact with the "ground" defined at $z = 0$

(**Fig. 20A**). If the dropped sphere comes into contact with a previously dropped sphere, it begins to roll longitudinally off of the sphere, we mimic this process by decreasing the angle between the center of the previously dropped sphere and the center of the dropping sphere (**Fig. 20B**). If the dropped sphere does not come into contact with a second dropped previously sphere as it is "rolling" around the previously dropped sphere, then it is dropped and the dropping process is repeated but with a new x-y "window." If the dropped sphere does come into contact with a second previously dropped sphere, it becomes tangent with both of the previously dropped spheres (**Fig. 20C**). At this point, the "fitting" process begins. The fitting process involves the dropped sphere going through a series of very small lateral and longitudinal rotations until the dropped sphere also becomes tangent to the floor or a third previously dropped sphere.
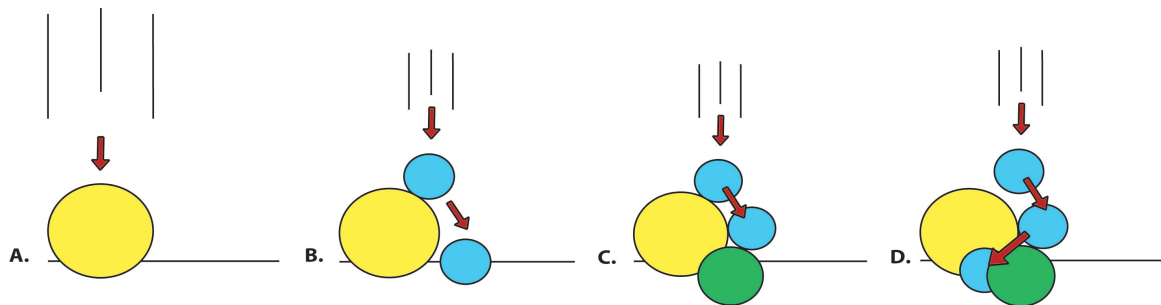

Fig. 20. A simplification of the sphere packing process. In this diagram the colored circles are used to represent particle spheres. (A) The yellow sphere drops to the floor at z = 0 and does not contact another sphere on its way down. (B) The blue sphere is dropped and makes contact with the yellow sphere. The blue sphere rolls tangentially around the yellow sphere until it is again dropped and then makes contact with the floor. (C) The blue sphere is dropped and again make contact with the yellow sphere. This time, as the blue sphere rolls tangentially down the yellow sphere, it makes contact with a second previously dropped sphere. The dropped blue sphere becomes tangent to both the yellow and the green sphere. (D) After the blue sphere becomes tangent to both the yellow and green spheres (C), the blue sphere will repeat a number of rotations that allow the dropped blue sphere to roll downwards while maintaining its tangencies to the two initially contacted spheres.

A sample of the results of such a sphere packing process is shown in **Fig. 21**. The

dropping, rolling, and fitting processes are intended to create a sphere packing that is

more natural than an idealized packing, with the additional benefit of not having to

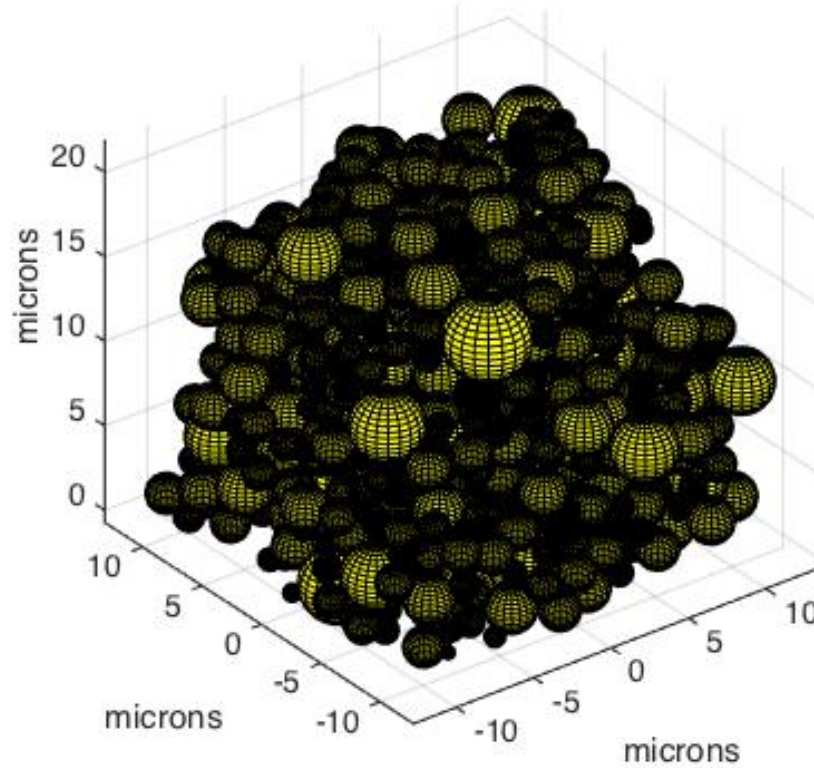explicitly characterize the geometry of each pore within the sphere packing.

Fig. 21. An example packing of spheres with $r_{mean} = 1\mu m$ and $\sigma = 0.5\mu m$ for a set of $n = 1000$ particles, which have radii that satisfy the PDF in **Fig. 16**. A cross-section at a chosen height can then be taken from the packing of heterogeneously sized spheres and used for testing. Much larger packings can be made, but this size of an assemblage is appropriate for displaying the results of the sphere packing process.

REFERENCES CITED

Bischof, J., Scherer, D., Herminghaus, S., Leiderer, P., 1996. Dewetting Modes of Thin Metallic Films: Nucleation of Holes and Spinodal Dewetting. Phys. Rev. Lett. 77, 1536–1539. doi:10.1103/PhysRevLett.77.1536

Cahn, J.W., Dash, J.G., Fu, H., 1992. Theory of ice premelting in monosized powders. J. Cryst. Growth 123, 101–108. doi:10.1016/0022-0248(92)90014-A

Clennell, M. Ben, Hovland, M., Booth, J.S., Henry, P., Winters, W.J., 1999. Formation of natural gas hydrates in marine sediments: 1. Conceptual model of gas hydrate growth conditioned by host sediment properties. J. Geophys. Res. 104, 22985. doi:10.1029/1999JB900175

Coxeter, H.S.M., 2002. The Problem of Apollonius. The American Mathematical Monthly 109, 5–15.

Collett, T.S., Riedel, M., Cochran, J., Boswell, R., Kumar, P., Sathe, A., NGHP Expedition 01 scientific party, 2008. Geologic controls on the occurrence of gas hydrates in the Indian continental margin : results of the Indian national gas hydrate program expedition 01. Proceedings of the 6th International Conference on Gas Hydrates (ICGH 2008).

Cook, A.E., Malinverno, A., 2013. Short migration of methane into a gas hydrate-bearing sand layer at Walker Ridge, Gulf of Mexico. Geochemistry, Geophys. Geosystems 14, 283–291. doi:10.1002/ggge.20040

Daigle, H., Dugan, B., 2011. Capillary controls on methane hydrate distribution and fracturing in advective systems. Geochemistry, Geophys. Geosystems 12. doi:10.1029/2010GC003392

Dash, J.G., Rempel, A. W., Wettlaufer, J.S., 2006. The physics of premelted ice and its geophysical consequences. Rev. Mod. Phys. 78, 695–741. doi:10.1103/RevModPhys.78.695

Davie, M., Zatsepina, O., Buffett, B., 2004. Methane solubility in marine hydrate environments. Mar. Geol. 203, 177–184. doi:10.1016/S0025-3227(03)00331-1

De Gennes, P.G., 1985. Wetting: Statics and Dynamics. Rev. Mod. Phys. doi:10.1103/RevModPhys.57.827

Denoyel, R., Pellenq, R.J.M., 2002. Simple phenomenological models for phase transitions in a confined geometry. 1: Melting and solidification in a cylindrical pore. Langmuir 18, 2710–2716. doi:10.1021/la015607n

Dewangan, P., Sriram, G., Ramprasad, T., Ramana, M.V., Jaiswal, P., 2011. Fault system and thermal regime in the vicinity of site NGHP-01-10, Krishna–Godavari basin, Bay of Bengal. Mar. Pet. Geol. 28, 1899–1914. doi:10.1016/j.marpetgeo.2011.03.009

Garvin, J.W., Udaykumar, H.S., 2006. Effect of a premelted film on the dynamics of particle-solidification front interactions. J. Cryst. Growth 290, 602–614. doi:10.1016/j.jcrysgro.2006.01.018

Hansen-Goos, H., Wettlaufer, J.S., 2010. Theory of ice premelting in porous media. Phys. Rev. E - Stat. Nonlinear, Soft Matter Phys. 81, 1–13. doi:10.1103/PhysRevE.81.031604

Israelachvili, J.N. Intermolecular and Surface Forces, 3rd Ed. Academic Press, 2011. ISBN: 978-0-12-391927-4

Kofke, D.A., 1993. Direct evaluation of phase coexistence by molecular simulation via integration along the saturation line. J. Chem. Phys. 98, 4149. doi:10.1063/1.465023

Laplace, P.S. Elementary illustrations of the Celestial mechanics of Laplace: part the first, comprehending the first book. London: Printed for J. Murray, 1821.

Liu, X., Flemings, P.B., 2011. Capillary effects on hydrate stability in marine sediments. J. Geophys. Res. Solid Earth 116, 1–24. doi:10.1029/2010JB008143

Lomba, E., Alvarez, M., Lee, L.L., Almarza, N.G., 1996. Phase stability of binary non-additive hard-sphere mixtures: A self-consistent integral equation study. J. Chem. Phys. 104, 4180. doi:10.1063/1.471229

Malinverno, A., Goldberg, D.S., 2015. Testing short-range migration of microbial methane as a hydrate formation mechanism: Results from Andaman Sea and Kumano Basin drill sites and global implications. Earth Planet. Sci. Lett. 422, 105–114. doi:10.1016/j.epsl.2015.04.019

Millington, R.J., Quirk, J.P., 1961. Permeability of porous solids. Trans. Faraday Soc. 57, 1200. doi:10.1039/tf9615701200

Mualem, Y., 1976. A new model for predicting the hydraulic conductivity of unsaturated porous media. Water Resour. Res. 12.

Or, D., & Hanks, R. J., 1992. Soil water and crop yield spatial variability induced by irrigation nonuniformity. Soil Science Society of America Journal, 56, 226-233. doi:10.2136/sssaj1992.03615995005600010035x

Or, D., Tuller, M., 1999. Liquid retention and interfacial area in variably saturated porous media: Upscaling from single-pore to sample-scale model. Water Resour. Res. 35, 3591–3605. doi:10.1029/1999WR900262

Rempel, A. W., Wettlaufer, J.S., Worster, M.G., 2001. Interfacial premelting and the thermomolecular force: thermodynamic buoyancy. Phys. Rev. Lett. 87, 088501. doi:10.1103/PhysRevLett.87.088501

Rempel, A. W., 2011. A model for the diffusive growth of hydrate saturation anomalies in layered sediments. J. Geophys. Res. 116, B10105. doi:10.1029/2011JB008484

Rempel, A. W., Worster, M.G., 1999. Interaction between a particle and an advancing solidification front. J. Cryst. Growth 205, 427–440. doi:10.1016/S0022-0248(99)00290-0

Rempel, A.W., 2012. Hydromechanical Processes in Freezing Soils. Vadose Zo. J. doi:10.2136/vzj2012.0045

Rose, K.K., Johnson, J.E., Torres, M.E., Hong, W.-L., Giosan, L., Solomon, E.A., Kastner, M., Cawthern, T., Long, P.E., Todd Schaef, H., 2014. Anomalous porosity preservation and preferential accumulation of gas hydrate in the Andaman accretionary wedge, NGHP-01 site 17A. Mar. Pet. Geol. 58, 99–116. doi:10.1016/j.marpetgeo.2014.04.009

Saarenketo, T., 1998. Electrical properties of water in clay and silty soils. J. Appl. Geophys. 40, 73–88. doi:10.1016/S0926-9851(98)00017-2

Tuller, M., Or, D., 2005. Water films and scaling of soil characteristic curves at low water contents. Water Resour. Res. 41. doi:10.1029/2005WR004142

Watanabe, K., Mizoguchi, M., 2002. Amount of unfrozen water in frozen porous media saturated with solution. Cold Reg. Sci. Technol. 34, 103–110. doi:10.1016/S0165-232X(01)00063-5

Wilder, J.W., Seshadri, K., Smith, D.H., 2001. Modeling hydrate formation in media with broad pore size distributions. Langmuir 17, 6729–6735. doi:10.1021/la010377y

Wilen, L.A., Wettlaufer, J.S., Elbaum, M., Schick, M., 1995. Dispersion-force effects in interfacial premelting of ice. Phys. Rev. B 52, 12426. doi:10.1103/PhysRevB.52.12426